Article

Click-locking strategy enables automated synthesis of single-atom catalysts with industrial compatibility

Weibin Chen[1,2], Long Feng[3], Bingbing Ma[1], Lina Zhang[4], Zhou Du[1,5], Fanqi Meng [1], Shengyao Wang [6] ✉, Shibo Xi[7], Xiao Hai [1], Ruiqin Zhong[3], Jin Zhang [1], Jiong Lu [8] ✉, Ju Li [2,9] ✉ & Ruqiang Zou [1,10] ✉

Developing scalable methods to synthesize single-atom catalysts (SACs) while maintaining high stability and activity remains a substantial challenge. Here, inspired by click chemistry, we propose a click-locking strategy that utilizes clicking auxiliaries to enable the synthesis of SACs. These clicking auxiliaries function as molecular 'click-locking seat belts', ensuring precise atomic anchoring, optimizing electronic structures and enhancing stability, while minimizing raw material loss. By integrating a robotic platform, we achieve high-throughput synthesis, generating extensive libraries of clicking-SACs and enabling rapid performance evaluation. This approach greatly accelerates the discovery of high-performance catalysts for electrocatalytic, photocatalytic and thermocatalytic processes. Furthermore, we demonstrate the kilogram-scale production of clicking-SACs, achieving exceptional catalytic activity and long-term stability. Extensive upscaling and stability tests validate the broad applicability and reliability of clicking-SACs, underscoring their potential as a transformative strategy in industrial catalysis.

Catalysts are essential for fostering global economic advancement[1,2], supporting over 90% of industrial chemical processes[3–5] and facilitating innovations in energy and environmental technologies[6]. As challenges such as climate change and resource depletion intensify, developing next-generation catalysts is crucial for achieving sustainable chemical transformations[7–10]. Extensive efforts have been made to shrink metal nanoparticles to the atomic scale, with the aim of maximizing the exposed surface area of metal catalysts while minimizing the consumption of raw material[11–15]. This has led to the emergence of single-atom

catalysts (SACs), in which individual metal atoms are uniformly dispersed on supports, ensuring full metal utilization with optimal atom economy[16–20]. However, the transition to industrial-scale applications of SACs encounters several notable challenges. One key issue is identifying optimal metal–support combinations tailored to specific catalytic processes[21–25]. A more pressing concern involves developing scalable, cost-efficient and time-effective synthesis methods that maximize production efficiency, minimize metal waste and maintain the uniform dispersion essential for high catalytic activity and durability[26–28].

[1]State Key Laboratory of Advanced Waterproof Materials, School of Materials Science and Engineering, Peking University, Beijing, China. [2]Department of Nuclear Science and Engineering, Massachusetts Institute of Technology, Cambridge, MA, USA. [3]State Key Laboratory of Heavy Oil Processing, China University of Petroleum, Beijing, China. [4]Department of Mechanical Engineering, Tsinghua University, Beijing, China. [5]SINOPEC (Beijing) Research Institute of Chemical Industry Co., Ltd. Yanshan Branch, Beijing, China. [6]School of Chemistry and Chemical Engineering, Shanghai Jiao Tong University, Shanghai, China. [7]Institute of Sustainability for Chemicals, Energy and Environment (ISCE2), Agency for Science, Technology and Research (A*STAR), Singapore, Singapore. [8]Department of Chemistry, National University of Singapore, Singapore, Singapore. [9]Department of Materials Science and Engineering, Massachusetts Institute of Technology, Cambridge, MA, USA. [10]School of Advanced Materials, Peking University Shenzhen Graduate School, Shenzhen, China. ✉e-mail: wangshengyao@sjtu.edu.cn; chmluj@nus.edu.sg; liju@mit.edu; rzou@pku.edu.cn

Traditional SAC synthesis methods primarily fall into direct synthesis approaches[29–32] (for example, coprecipitation[33,34]) and impregnation techniques[35,36]. While impregnation methods are commonly used due to their simplicity, they often result in substantial losses of metal precursors and are prone to agglomeration under thermal or chemical stress, posing substantial challenges to achieving high atom economy, catalytic activity and scalability[37–40]. Direct synthesis approaches, on the other hand, struggle to embed single atoms uniformly, often leading to compromised dispersion and diminished catalytic performance[37,41,42]. These limitations underscore the urgent need for effective synthesis strategies capable of addressing these bottlenecks and paving the way for the industrialization of SACs.

To overcome this challenge, we developed a strategy using clicking auxiliaries as 'click-locking seat belts' to anchor metal atoms, prevent agglomeration and minimize precursor loss. This approach enables precise atomic control while reducing metal ion loss. The versatility and efficiency of this approach were validated through integration with a robotic platform for high-throughput synthesis and testing, enabling the rapid preparation and screening of clicking-single-atom catalysts (C-SACs). Selected catalysts exhibited outstanding performance in various electrocatalytic and photocatalytic reactions, including the hydrogen evolution reaction (HER), oxygen evolution reaction (OER), carbon dioxide reduction reaction (CO_2RR), NO reduction reaction (NORR) and urea oxidation reaction (UOR). Even more promisingly, the scalability of the C-SAC concept was demonstrated using a scaled-up reactor. These catalysts underwent evaluation across critical reactions, such as CO oxidation, NO_x removal and CO_2 hydrogenation, showcasing exceptional activity, selectivity and long-term durability.

Definition of clicking-single-atom catalysts

Inspired by the principles of click chemistry[43–46], we present a strategy for the precise assembly of single atoms and support materials, analogous to constructing SACs from well-defined building blocks (Supplementary Fig. 1). This method transforms supports into 'clicking blocks' through surface modifications that create high-affinity sites for single metal atoms, ensuring stable anchoring (Supplementary Fig. 2). Conventional SAC synthesis often relies on weak metal–support interactions, leading to limited durability (Fig. 1a). By contrast, our approach employs clicking auxiliaries to secure single atoms onto supports with enhanced stability. This design enables high-throughput synthesis (Fig. 1b) and supports scale-up production (Fig. 1c). The synthesis is driven by forces such as electrostatic attraction, further amplified by clicking auxiliaries. We establish criteria for C-SAC synthesis, including rapid fabrication, scalability, stability and reliance on accessible materials (details are provided in Supplementary Note 1).

Clicking auxiliaries for atomic anchoring

Clicking auxiliaries play a critical role in the synthesis of C-SACs by providing a driving force that ensures the stable and site-specific anchoring of single atoms onto the support. Here we demonstrate Coulomb attractions (electron–cation interaction) as a representative click-driving force, showcasing its role in facilitating stable anchoring. Clicking auxiliaries impart negative charges to neutral supports, facilitating the anchoring and loading of metal ions (M^{n+}), as illustrated in Fig. 2a. The electronic structure of the clicked support is fine-tuned to form compatible bonding orbitals that align with the metal orbitals, ensuring strong metal–support interactions. By contrast, the unclicked supports result in a weak bonding state between the metal and the support.

In this study, we propose using electron-donating agents (Supplementary Fig. 3)—such as VC (vitamin C; $C_6H_8O_6$)—as clicking auxiliaries to effectively anchor metal ions. Taking VC as an example, with CeO_2 as the support, we detail the VC conversion mechanism and electron transfer process (Fig. 2b). Starting from isolated VC and pristine CeO_2 (reference state, energy = 0 eV), VC initially physisorbs onto

CeO_2 via hydrogen bonding (−0.23 eV). Chemisorption then occurs through hydrogen transfer to form surface hydroxyl groups (−1.45 eV; 0.63 electrons transferred). The VC is oxidized to dehydroascorbic acid (DHA; $C_6H_6O_6$) with another hydrogen transfer process, stabilizing the system further to −2.94 eV, with a total of 0.84 electrons transferred to CeO_2. Subsequently, DHA desorbs under mild conditions, further reducing the energy to −3.25 eV, thus generating a stable electron-rich CeO_2 surface. Proton nuclear magnetic resonance (^{1}H NMR) spectroscopy confirmed VC-to-DHA conversion by comparing initial and post-reaction VC solutions with CeO_2 (Fig. 2c). The disappearance of VC proton signals (H_a, 4.90 ppm) and emergence of DHA signals (H_b, 4.60 ppm)[47] confirmed the completed conversion process of VC[48]. To confirm the removal of VC and DHA after electron transfer, we conducted ^{1}H NMR spectroscopic analysis on both the final washing filtrate and the subsequent rinse solution. As shown in Fig. 2c, only water peaks were detected, with no signals from residual organics, indicating total removal of VC and DHA from the surface of CeO_2. Elemental analysis of carbon content (Supplementary Fig. 4) further supports this conclusion, demonstrating that our washing protocol effectively eliminates residual clicking auxiliaries post-electron transfer.

We provide comprehensive experimental validation supporting the formation and stability of an electron-rich state on CeO_2 surfaces following VC removal. Raman spectroscopy (Supplementary Fig. 5) clearly demonstrates that introducing VC substantially reduces the intensity and causes a redshift of the CeO_2 F_{2g} vibrational mode (~465 cm^{-1}). These spectral changes correspond to increased Ce^{3+} species, indicative of an electron-rich state[49–52]. Furthermore, the X-ray photoelectron spectroscopy (XPS) analysis (Fig. 2e) shows a substantial increase in Ce^{3+} content, rising from 18.1% (pristine CeO_2) to 29.5% after VC adsorption[53,54]. Remarkably, even after extensive washing, the Ce^{3+} content remains elevated at 27.3%, highlighting the irreversibility of electron transfer from VC to the CeO_2 surface[55]. Additionally, O 1s XPS spectra reveal a persistent negative shift in oxygen-binding energy following washing (Fig. 2f), confirming sustained electron enrichment around oxygen atoms[56]. As shown in Supplementary Fig. 6a, UV–visible diffuse reflectance spectroscopy reveals that both CeO_2-VC and CeO_2-VC-2 exhibit pronounced tail absorption in the visible region, which is typically associated with structural disorder, oxygen vacancies or electron-rich surfaces[55,57]. However, complementary analyses— including X-ray diffraction (XRD) (Supplementary Fig. 6b), Rietveld refinement (Supplementary Fig. 7) and electron paramagnetic resonance (EPR) spectroscopy (Supplementary Fig. 6c)—rule out structural disorder, changes in lattice parameters and the formation of oxygen vacancies for CeO_2. These findings confirm that the observed tail absorption primarily arises from sustained electron enrichment due to electron transfer from VC. Collectively, these results demonstrate the stability of the electron-rich CeO_2 surface even after removal of the VC or DHA[58,59].

Ab initio molecular dynamics (AIMD) simulations offer an intuitive depiction of the energy landscape evolution during the synthesis of C-SACs enabled by clicking auxiliaries. In the Cu_1/CeO_2 system, direct adsorption of Cu^{2+} onto the unmodified CeO_2 surface faces a high energy barrier (1.60 eV; Supplementary Fig. 8a). By contrast, the presence of clicking auxiliaries substantially lowers the overall energy barriers throughout the process. Specifically, VC chemisorbs onto the CeO_2 surface with a barrier of 0.63 eV (Supplementary Fig. 8b), during which it donates electrons to CeO_2 and is oxidized to DHA, which is subsequently removed by washing, and residual surface protons are then removed with a barrier of 0.82 eV (Supplementary Fig. 8c), forming stable, negatively charged anchoring sites. Cu^{2+} ions subsequently migrate and anchor electrostatically at these sites with a low barrier of 0.45 eV (Supplementary Fig. 8d). Stability tests confirm the formation of strong metal–support interactions that remain intact at 800 K (Supplementary Fig. 8e). The generality of this anchoring strategy was demonstrated with Fe^{3+} and Pt^{2+} ions, which anchored
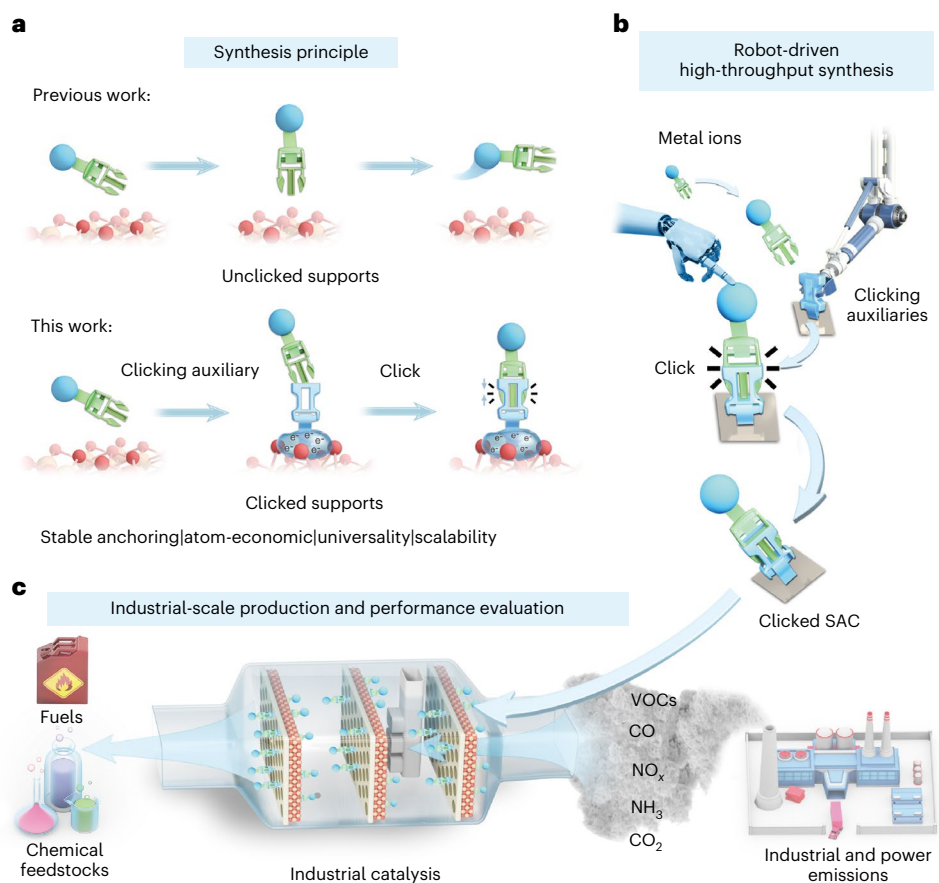
Fig. 1 | Conceptual illustration of clicking-single-atom catalysts. Illustration of the scientific principles underlying the concept of clicking-single-atom catalysts. **a**, The precise and strong anchoring of single atoms via atom-click synthesis, inspired by click chemistry, differs from traditional SAC synthesis methods relying on weaker metal–support interactions. **b**, The high-throughput capability of the robot-driven synthesis process, enabling efficient exploration of compositional and structural spaces. **c**, The scalability of this method and its potential applications in industrial catalysis, particularly for energy and chemical transformations. VOCs, volatile organic compounds.

onto electron-rich CeO_2 surfaces with relatively low energy barriers (0.90 eV and 1.18 eV, respectively; Supplementary Fig. 9). Furthermore, the approach generalizes effectively to TiO_2 supports (Supplementary Fig. 10).

High-throughput C-SAC synthesis

To transition from proof-of-concept of C-SACs to practical implementation, the development and scalability of C-SACs necessitate integration of high-throughput synthesis capabilities. These metrics are critical for achieving industrial viability, enabling reproducibility and accelerating the optimization of catalyst preparation and testing workflows[16,60,61]. The modular design of the C-SAC synthesis method renders it ideally suited for robot-driven platforms, providing substantial advantages in efficiency and consistency. The modular nature of the C-SAC synthesis is demonstrated by producing two catalyst categories—powder-based and electrode-supported—each requiring distinct protocols.

For the synthesis platforms designed for powder-based samples, as illustrated in Fig. 3a, a liquid-handling robot (Supplementary Fig. 11a) selected materials from curated libraries. These libraries included supports (for example, CeO_2 and TiO_2), clicking auxiliaries (for example, VC) and metal salt solutions (for example, copper nitrate), enabling precise and efficient preparation of the synthesis components. The platform efficiently integrates these components into modular workflows under programmatic control. Supplementary Fig. 11b illustrates the functional zones of the platform, while Supplementary Fig. 11c–e displays custom-designed, three-dimensional (3D)-printed sample

holders for enhanced handling. Additionally, Supplementary Fig. 11f–h shows photographs of the candidate libraries for support, clicking auxiliaries and metal precursors, emphasizing the practical implementation of this approach.

In this demonstration, CeO_2-(111) and CeO_2-(110) supports were functionalized with VC (Supplementary Fig. 11i,j), followed by anchoring of Cu^{2+} onto the modified surfaces. As illustrated in Fig. 3b, VC chemisorbs onto CeO_2 and is oxidized to DHA, which is subsequently removed by the washing process. This process leaves behind stable, negatively charged sites ideal for anchoring metal ions, such as Cu^{2+}. Both theoretical calculations and experimental results confirm that the electron-enriched CeO_2 surface enables stable single-atom anchoring (Supplementary Note 2, Supplementary Fig. 12 and Supplementary Table 1). We selected CeO_2 as the support primarily because its exposed (111) surface presents substantial challenges for anchoring Cu^{2+}, due to symmetry mismatch and limited orbital overlap—resulting in large energy gaps between interacting orbitals (Supplementary Fig. 13). As such, synthesizing SACs on this inert surface remains challenging (Supplementary Note 3). This highlights the advantage of the clicking-auxiliary strategy in addressing these inherent limitations (Supplementary Figs. 14–22).

Comprehensive characterizations were conducted to validate the successful synthesis of the designed C-SACs and to demonstrate the efficacy of the clicking-auxiliary strategy. Inductively coupled plasma optical emission spectroscopy (ICP-OES) analysis confirmed efficient Cu anchoring, with Cu_1/CeO_2-(111) exhibiting a Cu loading of 4.31 wt%.
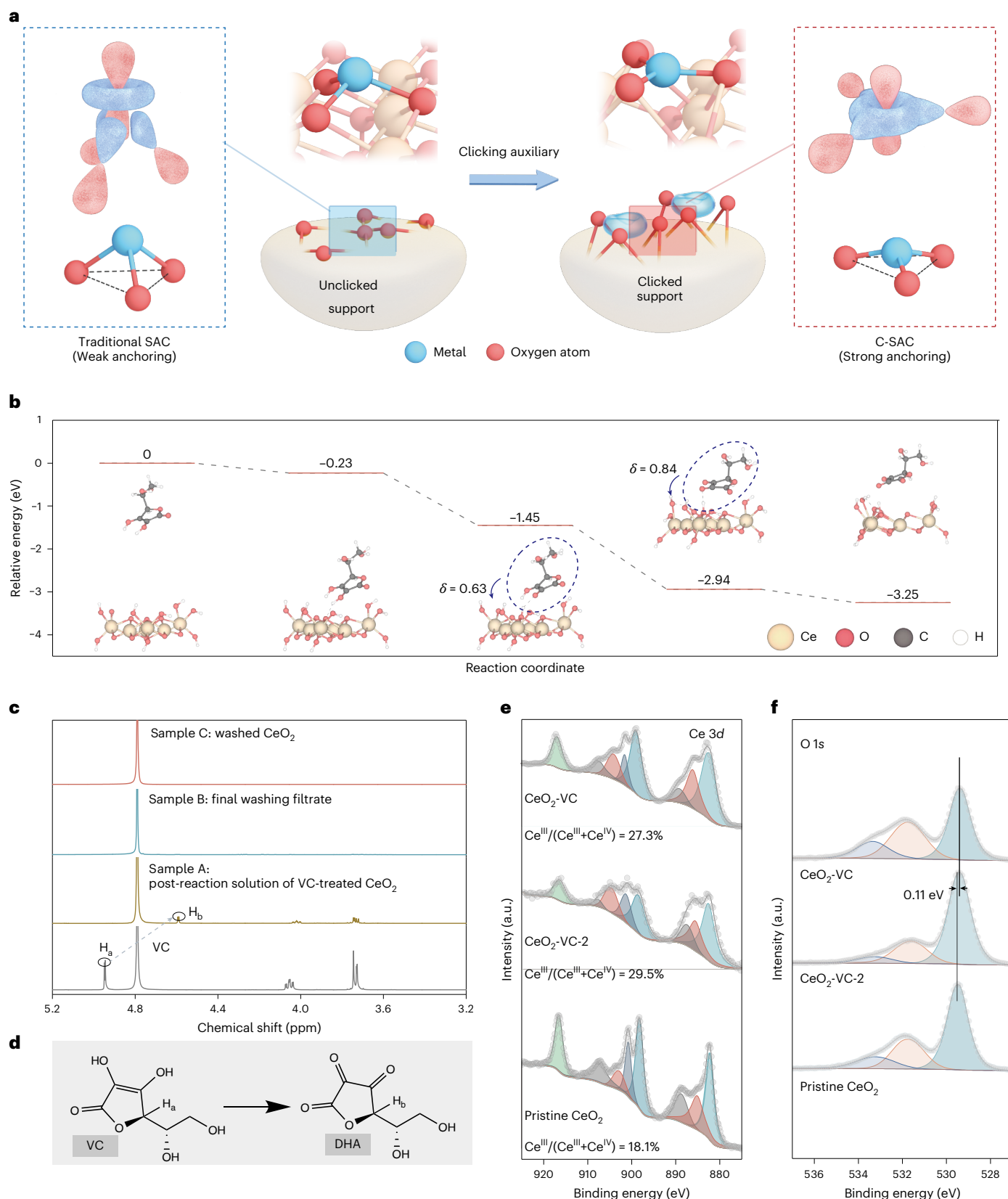
Fig. 2 | Theoretical and experimental investigation of clicking auxiliaries for C-SAC synthesis. a, Schematic representation of the preparation strategy for C-SACs using clicking auxiliaries, highlighting their role in stabilizing single-atom anchoring through electron donation. **b**, Reaction pathway and energy profile of the interaction between VC and CeO_2. The electron transfer (δ) is the net charge transferred from VC to CeO_2, referenced to isolated VC and pristine CeO_2. **c**, ^{1}H NMR spectra of pure VC (grey), sample A (post-reaction solution of VC-treated CeO_2, brown), sample B (final washing filtrate, blue) and sample C (rinse solution, red). **d**, Molecular structures of VC and DHA illustrating the specific H_a and H_b proton positions corresponding to peaks observed in the ^{1}H NMR spectra. **e**,**f**, XPS spectra of the Ce 3d (**e**) and O 1s (**f**) regions for pristine CeO_2, CeO_2-VC-2 (VC-treated for 2 min, without washing) and CeO_2-VC (VC-treated for 2 min, followed by thorough washing).
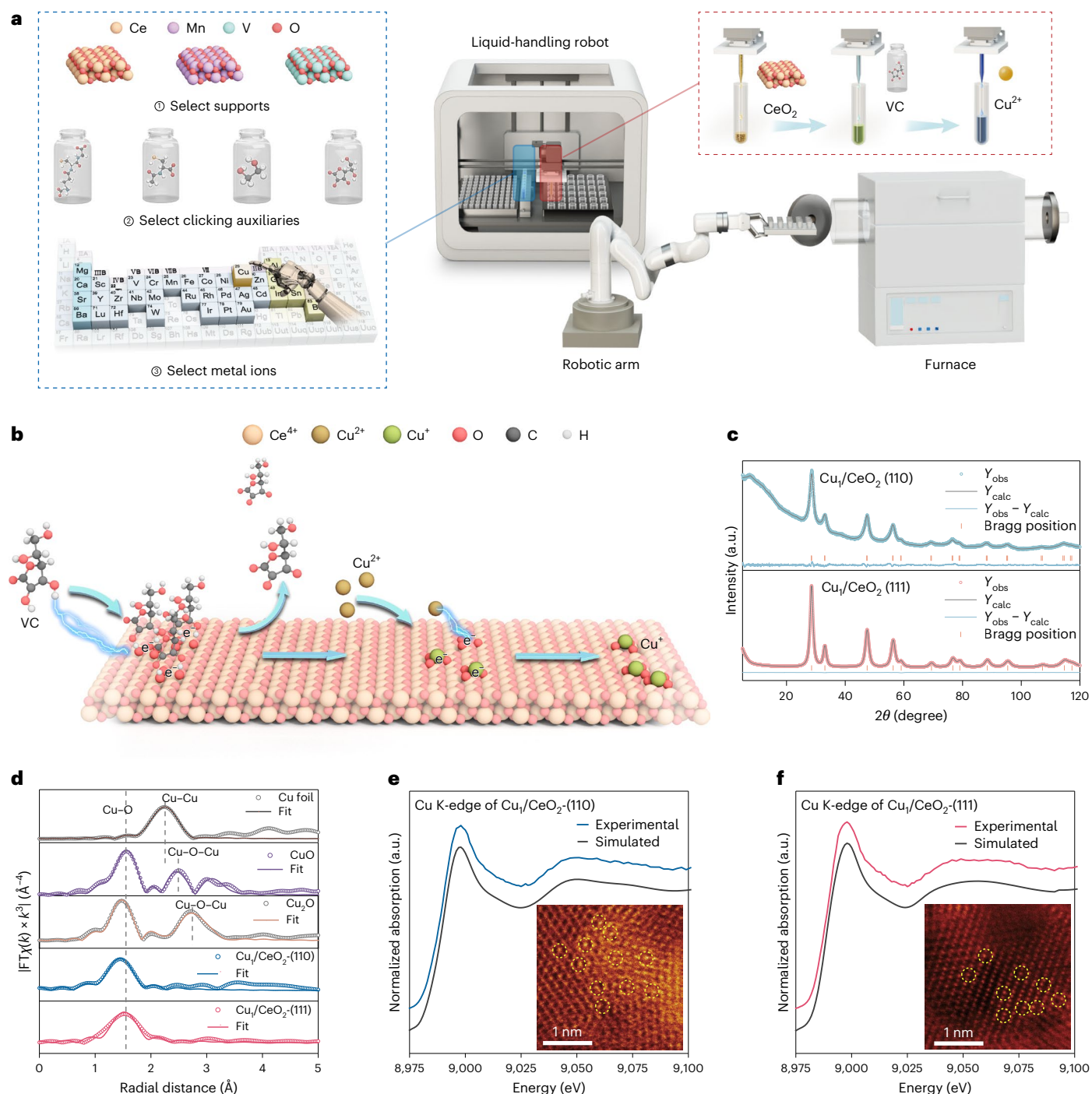
Fig. 3 | High-throughput synthesis, mechanism and characterization of C-SACs using Cu_1/CeO_2 as a model system. a, Robotic automated synthesis platform integrating a liquid-handling robot and a six-axis robotic arm, systematically combining materials from curated libraries of supports, clicking auxiliaries and metal precursors. **b**, Schematic representation of the synthesis mechanism using CeO_2 as the support, Cu^{2+} as the metal precursor and VC as clicking auxiliary. The process includes VC chemisorption onto CeO_2, electron donation from VC to CeO_2, oxidation of VC to DHA and subsequent removal of residual VC and DHA via washing, creating stable negatively charged surface sites ideal for metal ion anchoring. **c**, XRD patterns of Cu_1/CeO_2 C-SACs with different exposed facets. Y_{obs}, the observed diffraction intensity measured experimentally; Y_{calc}, the calculated diffraction intensity generated from the structural model based on the current refinement parameters. **d**, k^3-weighted Cu K-edge FT-EXAFS spectra and the fit for Cu_1/CeO_2 C-SACs, with Cu foil, CuO and Cu_2O as references. FT, Fourier transform; $\chi(k)$, the normalized EXAFS oscillation; k, the magnitude of the photoelectron wave vector (momentum transfer) relative to the absorption edge energy. **e,f**, Experimental XANES spectra compared with the calculated XANES data of optimized DFT-modelled structure of Cu_1/CeO_2 C-SACs with different exposed crystal facets: Cu_1/CeO_2-(110) (**e**) and Cu_1/CeO_2-(111) (**f**). Insets: the corresponding atomic-resolution HAADF-STEM images of Cu_1/CeO_2-(110) and Cu_1/CeO_2-(111).

By contrast, the absence of clicking auxiliaries resulted in a significant reduction in Cu loading of approximately 0.82 wt% in Cu_x/CeO_2-1 (Supplementary Table 1). Transmission electron microscopy (TEM) imaging of Cu_1/CeO_2-(111) (Supplementary Fig. 23 and Supplementary

Note 4) revealed well-dispersed Cu species with no detectable nanoparticle or cluster formation.

To elucidate the atomic dispersion of Cu, XRD patterns of Cu_1/CeO_2-(111) and Cu_1/CeO_2-(110) exclusively displayed diffraction

peaks corresponding to the cubic fluorite phase of CeO_2, without any secondary peaks attributable to Cu or CuO_x species (Fig. 3c and Supplementary Table 2). The X-ray absorption spectra provided compelling evidence regarding the nature of the Cu species. The extended X-ray absorption fine structure (EXAFS) spectra (Fig. 3d) confirmed the presence of atomically dispersed Cu and showed no evidence of Cu–Cu scattering paths in any of the two Cu_1/CeO_2 C-SAC samples. To further validate the atomic coordination of the Cu sites, first-principles calculations were conducted to model the configurations and simulate their corresponding X-ray absorption near-edge structure (XANES) spectra. The proposed configurations of the C-SACs show perfect agreement with the experimental Cu K-edge XANES spectrum of Cu_1/CeO_2-(110) (Fig. 3e) and Cu_1/CeO_2-(111) (Fig. 3f), respectively. The corresponding atomic-resolution high-angle annular dark-field scanning transmission electron microscopy (HAADF-STEM) images of Cu_1/CeO_2-(110) (inset of Fig. 3e) and Cu_1/CeO_2-(111) (inset of Fig. 3f) further confirmed the introduction of copper in a single-atom distribution. To substantiate this observation, additional HAADF-STEM imaging of Cu_1/CeO_2-(111) was performed (Supplementary Fig. 24a–c), which consistently showed the presence of isolated bright spots attributed to single Cu atoms. To unequivocally confirm that these bright spots corresponded to single Cu atoms, atomic-scale electron energy loss spectroscopy and elemental mapping were conducted on Cu_1/CeO_2-(111) (Supplementary Fig. 24d). The electron energy loss spectroscopy analysis identified a pronounced Cu K-edge signal at the precise locations of the bright spots, providing direct evidence for the single-atom nature of the Cu species.

To exclude alternative Cu stabilization pathways, we first performed control experiments by mixing VC with copper nitrate in the absence of CeO_2. EXAFS analysis of the resulting Cu-VC complex revealed distinct Cu–Cu scattering features at ~2.1–2.5 Å (Supplementary Fig. 25), indicative of metallic bonding. This demonstrates that VC alone cannot stabilize single Cu atoms. Furthermore, to rule out the formation of CeO_2-supported M–N–C-type single-atom configurations, we constructed theoretical models of metal–nitrogen coordination on CeO_2 and simulated their XANES spectra. The calculated spectra showed substantial deviation from the experimental Cu K-edge XANES of Cu_1/CeO_2-(111) (Supplementary Fig. 26), definitively excluding this structure. Detailed discussions of Supplementary Figs. 25 and 26 are provided in Supplementary Note 5.

In addition to the above-mentioned Cu_1/CeO_2-(111), we successfully synthesized multiple C-SAC samples (Supplementary Table 3). Given the large number of samples, performing comprehensive characterization on all of them was both time-intensive and resource-demanding. Instead, a subset of the synthesized samples was selected for detailed analysis. XPS spectra (Supplementary Fig. 27) confirmed the presence of active metal species, indicating their successful anchoring. XRD patterns of Cu-based C-SACs (Supplementary Fig. 28) and TiO_2-based C-SACs (Supplementary Fig. 29) showed only peaks corresponding to the supports, without signals indicative of Cu or noble metal clusters. Atomic-resolution HAADF-STEM imaging (CeO_2-based C-SACs in Supplementary Fig. 24e–g; TiO_2-based C-SACs in Supplementary Fig. 30) confirmed the presence of isolated single atoms. Additionally, EXAFS spectra of the selected samples exhibited prominent peaks around 1.5–2.0 Å, attributed to M–O bond lengths, with no evidence of metal–metal coordination between 2.1 Å and 2.5 Å (Supplementary Fig. 31). These findings conclusively confirmed the absence of metal nanoparticles or clusters, demonstrating the successful formation of C-SACs[62–65].

Catalytic performance evaluation with high-throughput automation

After producing a substantial quantity of catalysts, we carried out a comprehensive evaluation of their catalytic performance. To demonstrate this workflow, we first synthesized a batch of electrode-based C-SACs optimized for electrocatalytic testing. Our initial step involves developing a robotic arm specifically designed for the activation and functionalization of C-SAC electrodes with the aid of a clicking auxiliary (Supplementary Fig. 32). The process involves magnetron sputtering of CeO_2 onto conductive substrates, such as nickel foam or carbon paper, followed by robotic immersion of the CeO_2-coated electrodes (CeO_2@NF) in a solution containing the clicking auxiliary of VC to form CeO_2-VC (CeO_2-VC@NF). Subsequently, the liquid-handling robot deposits metal precursors onto the functionalized surface (Supplementary Fig. 33). As shown in Fig. 4a, this streamlined platform enables high-throughput, automated catalyst synthesis, allowing programmatically controlled exploration of the catalyst space with exceptional efficiency and reproducibility.

Furthermore, a robotic-driven system was established for evaluating electrochemical performance (Supplementary Fig. 34). The platform exhibited excellent batch-to-batch consistency and operational stability, as detailed in Supplementary Note 6, Supplementary Fig. 35 and Supplementary Table 4. Using this system, over 100 C-SAC-based electrodes were screened (Supplementary Tables 5–7), resulting in the identification of several high-performance electrocatalysts. For instance, the Pt_1/CeO_2-VC@NF catalyst achieved a current density of 100 mA cm^{-2} at an overpotential of 48.4 mV for HER (Fig. 4b), outperforming the majority of previously reported catalysts (Supplementary Table 8). Similarly, Fe_1/CeO_2-VC@NF required only 306.7 mV to achieve 100 mA cm^{-2} for OER (Fig. 4c and Supplementary Table 9), while Ni_1/CeO_2-VC@NF surpassed state-of-the-art UOR benchmarks (Fig. 4d and Supplementary Table 10). The Tafel slopes clearly illustrate the catalytic kinetics, with Pt_1/CeO_2-VC@NF (Supplementary Fig. 36a), Fe_1/CeO_2-VC@NF (Supplementary Fig. 36b) and Ni_1/CeO_2-VC@NF (Supplementary Fig. 36c) demonstrating efficient HER, OER and UOR activities, respectively. Selecting UOR as a representative case, we performed computational analyses to elucidate the catalytic mechanism (see Supplementary Fig. 37 and Supplementary Note 7 for details).

In addition to electrocatalytic activity, the C-SACs also exhibit good photocatalytic performance. When using TiO_2 as the support, Cu_1/TiO_2 C-SACs achieved high activities in both photocatalytic CO_2 reduction (Supplementary Fig. 38), achieving 893 μmol g^{-1} CO over 5 h and NO reduction (Supplementary Fig. 39), achieving 251 μmol g^{-1} NH_3 over 5 h. Additionally, for the photocatalytic hydrogen evolution reaction, the Pt_1/TiO_2 C-SACs demonstrated exceptional activity, achieving 77.5 mmol g^{-1} over 5 h (Supplementary Fig. 40). These encouraging results underscore the transformative potential of our automated C-SAC platform.

Scale-up synthesis and thermal catalysis evaluation

Having established a robotic-driven platform that accelerates C-SAC discovery, we next sought to scale up C-SAC synthesis and validate its industrial feasibility. As shown in Fig. 5a, before large-scale production, we proposed a workflow combining theoretical computation and high-throughput screening to identify promising single-metal centres for targeted thermal catalytic reactions. In this demonstration, we focused on pollutant mitigation from the combustion of coal and oil emissions (CO, NO_x and residual NH_3) (Supplementary Figs. 41–43 and Supplementary Note 8). Through this approach, we identified Cu_1/CeO_2 C-SACs as highly promising candidates. In thermal catalytic CO oxidation tests, Cu_1/CeO_2-(111) and Cu_1/CeO_2-(110) achieved 50% conversion at just 125 °C, substantially outperforming non-clicked counterparts (Fig. 5b). Density functional theory (DFT) calculations revealed that single Cu atoms act as active sites, enhancing CO adsorption and intermediate formation while reducing reaction energy barriers (Supplementary Fig. 44; details are provided in Supplementary Note 9). For NH_3-selective catalytic reduction (SCR), the Cu_1/CeO_2-(111) maintained NO conversion above 95% and N_2 selectivity above 95% across 150–240 °C (Fig. 5c). NH_3-temperature programmed desorption (NH_3-TPD) and O_2-TPD data revealed
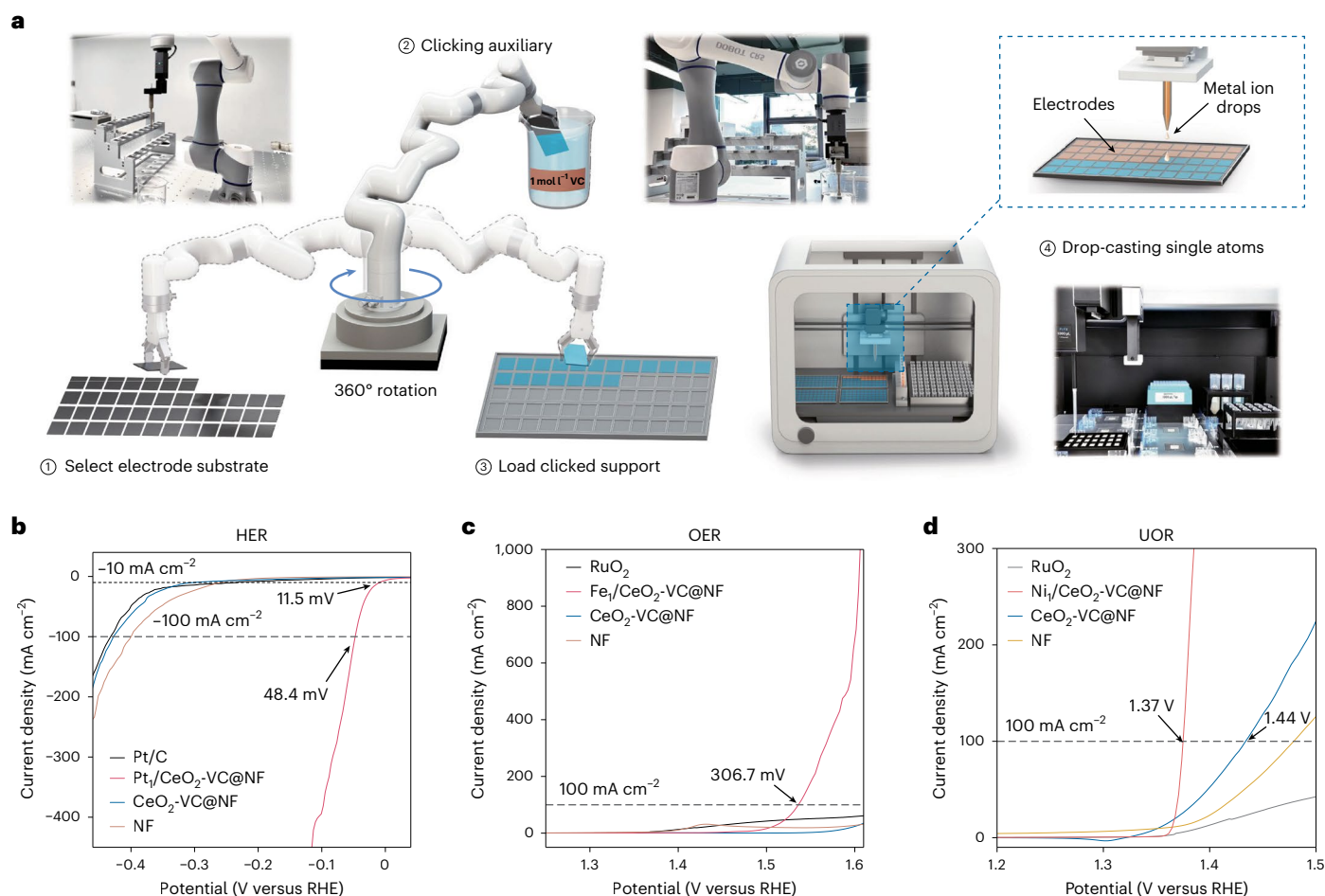
Fig. 4 | Robotic-driven, high-throughput synthesis and performance evaluation of electrode-based C-SACs. a, Schematic representation of the robotic synthesis route for C-SAC-based electrocatalysts. **b**–**d**, Catalytic performance of representative C-SACs: electrocatalytic HER (**b**), OER (**c**) and UOR (**d**). NF, nickel foam; RHE, reversible hydrogen electrode.

that Cu_1/CeO_2-(111) substantially enhanced NH_3 and O_2 adsorption (Supplementary Fig. 45). Theoretical studies showed enhanced kinetics for NH_3 dissociation and H^* removal, reducing the barriers from 0.95 eV to 0.58 eV and 1.01 eV to 0.70 eV, respectively (Supplementary Figs. 46–55; details are provided in Supplementary Note 10).

We successfully scaled up C-SAC synthesis to 100-litre reactors (Fig. 5d), achieving yields exceeding 10 kg of C-SACs (Fig. 5e). XANES and EXAFS analyses confirmed that Cu remained atomically dispersed (Supplementary Figs. 56 and 57 and Supplementary Table 11; details are provided in Supplementary Note 11). Long-term stability tests in CO_2 hydrogenation demonstrated the robustness of the C-SACs under operational conditions (Supplementary Fig. 58a). Specifically, Cu_1/CeO_2-(111)-L catalysts were rigorously tested over a 350-hour thermal catalytic CO_2 hydrogenation trial, showcasing their remarkable stability throughout this period. The catalyst consistently maintained a CO_2 conversion rate exceeding 20% and achieved a high methanol selectivity. By contrast, the Cu-VC/CeO_2 and Cu_x/CeO_2-2 catalysts showed inferior performance. Cu/CeO_2-H_2 showed even poorer activity (<10% conversion and <5% methanol selectivity), underscoring the superiority of the C-SAC strategy over conventional H_2-treatment approaches. These impressive outcomes highlight the ability of Cu_1/CeO_2-(111)-L to sustain high methanol selectivity while resisting deactivation mechanisms, such as sintering and poisoning, even under prolonged operational conditions, making them exceptionally promising for industrial-scale CO_2 hydrogenation to methanol. Furthermore, Cu_1/CeO_2-(110)-L sustained over 80% CO conversion during a thorough 70-hour testing period for

the CO oxidation reaction (Fig. 5f). This aligns with previous studies showing that H_2O positively influences CO oxidation on CeO_2-based catalysts[23,66,67]. Moreover, a reversible enhancement in CO conversion was also observed in the presence of H_2O, further validating the robustness of Cu_1/CeO_2-(110)-L. In addition, the Cu_1/CeO_2-(111)-L achieved over 95% NO conversion at 240 °C, maintaining this performance for nearly 80 h in the NH_3-SCR reaction (Fig. 5g).

To illustrate the environmental and economic advantages of the C-SAC synthesis method, we conducted comprehensive cradle-to-gate lifecycle assessments and techno-economic analysis, using Cu_1/CeO_2-(111)-L as a representative case. The environmental footprint and production cost of Cu_1/CeO_2-(111) C-SACs were benchmarked against commercial V–W–Ti catalysts commonly employed in NH_3-SCR applications. Our analysis clearly demonstrates that Cu_1/CeO_2-(111) C-SACs possess substantially reduced environmental impacts and lower associated costs compared to traditional V–W–Ti catalysts, highlighting the substantial advantages and practical feasibility of this synthesis approach (Supplementary Fig. 59; detailed analysis available in Supplementary Note 12). Finally, we evaluated C4 fraction hydrogenation using real industrial feedstocks, and the catalytic performance is summarized in Supplementary Fig. 60, Supplementary Table 12 and Supplementary Note 13.

Discussion

This work introduces the concept of C-SACs—a distinct class of catalysts synthesized via a click-chemistry-inspired approach. By leveraging
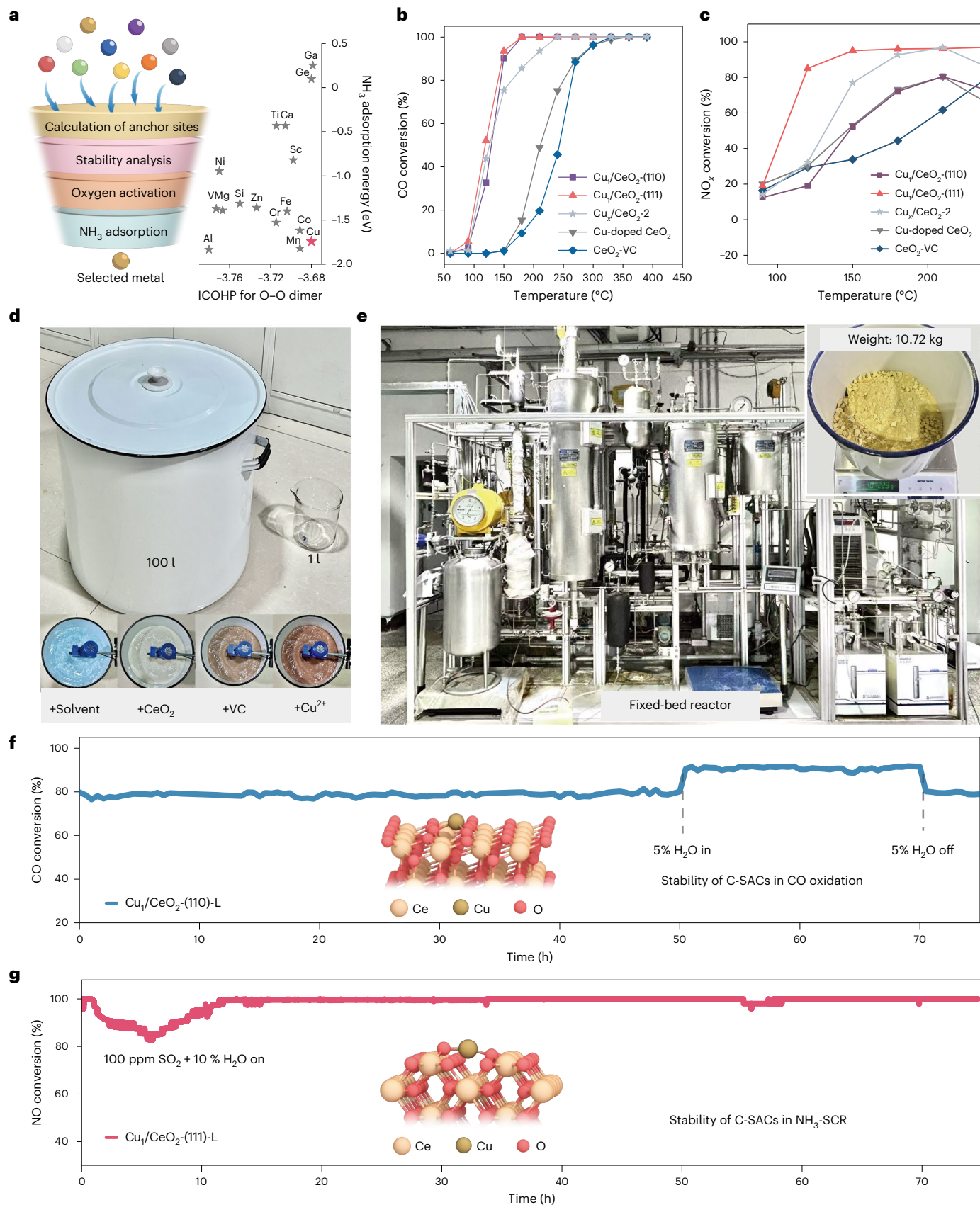
Fig. 5 | Catalytic performance evaluation of C-SACs. a, Theoretical screening of candidate C-SACs for optimal activity in NO_x removal (via NH_3-SCR) and CO oxidation. ICOHP, integrated crystal orbital Hamilton population. **b**, Catalytic activity for CO oxidation over Cu_1/CeO_2-(110), Cu_1/CeO_2-(111), Cu-doped CeO_2, Cu_x/CeO_2-2 and CeO_2-VC. **c**, NO conversion performance over Cu_1/CeO_2-(110), Cu_1/CeO_2-(111), Cu-doped CeO_2, Cu_x/CeO_2-2 and CeO_2-VC under NH_3-SCR conditions. **d**, Photograph of scaled-up C-SAC synthesis in a 100-litre reactor. **e**, Photograph of a representative fixed-bed reactor. **f**, Stability evaluation of CO oxidation activity over the Cu_1/CeO_2-(110)-L catalyst, including a 20-hour period (50–70 h) with 5 vol.% H_2O introduced in the feed. **g**, Stability evaluation of NH_3-SCR performance over the Cu_1/CeO_2-(111)-L catalyst at 180 °C.

clicking auxiliaries to stably anchor single atoms onto supports while fine-tuning their electronic structures, we address critical barriers that have impeded the transition of single-atom catalysis from laboratory research to industrial application. In particular, we demonstrate a high-throughput synthesis platform for rapid screening and successful kilogram-scale production in industrial reactors. This methodology enables the creation of a comprehensive C-SAC library, including catalysts previously considered unfeasible on industrially inert supports. The resulting C-SACs exhibit outstanding performance in electrocatalysis, photocatalysis and thermal catalysis, coupled with exceptional stability and resistance to poisoning under realistic operational conditions. These findings highlight the durability (through stable anchoring), atom economy, universality and scalability of C-SACs in demanding production environments and underscore their transformative potential in modern catalysis. Moreover, the modular, robot-driven high-throughput workflow enables data-rich, artificial intelligence-assisted C-SAC discovery, paving the way for closed-loop optimization and autonomous C-SAC design.

Methods

High-throughput synthesis of powder-based C-SACs

We established a robotic system for synthesizing of C-SAC powders, integrating a liquid-handling robot (Opentrons Flex; Supplementary Fig. 11a,b) with a robotic arm and a furnace. A custom-designed six-tube rack (Supplementary Fig. 11c), fabricated via 3D printing, accommodates centrifuge tubes containing various support materials and clicking auxiliaries. For example, CeO_2 slurries (Supplementary Fig. 11f) serve as support materials, while VC solutions (Supplementary Fig. 11h) function as clicking auxiliaries. A 15-channel rack (Supplementary Fig. 11d), also 3D-printed, houses centrifuge tubes for storing diverse metal precursor solutions (Supplementary Fig. 11g). Additionally, a specially designed 15-tube rack compatible with an oscillatory mixing module facilitates the automated and uniform mixing of supports, auxiliaries and precursors. The Opentrons Flex liquid-handling robot is equipped with P1000S GEN3 and P1000M GEN3 pipette modules, enabling precise single-channel and multichannel liquid handling. Its integrated Heater–Shaker module provides thorough mixing under controlled temperature conditions, while the Temperature module ensures stable storage of temperature-sensitive reactants. Automation scripts are generated via the Hardware Executor and seamlessly uploaded through a desktop application or Jupyter notebook.

The synthesis of Cu_1/CeO_2 C-SACs, including Cu_1/CeO_2-(111) and Cu_1/CeO_2-(110), is presented as a representative demonstration of the preparation process. First, 0.4 g CeO_2 with (111) facet-exposed powder[68] or CeO_2-(110) facet-exposed powder[69], prepared following previously established methods, was dispersed in 40 ml of deionized water to form a CeO_2 suspension. Separately, 240 mg of VC was dissolved in 40 ml deionized water to yield a 34 mM solution. Both suspensions were stored in 50-ml tubes on a temperature-controlled rack. The liquid-handling robotic system transferred ~3 ml of the CeO_2 suspension into a reaction tube on the Heater–Shaker module (Supplementary Fig. 11i), ensuring uniform dispersion through gentle mixing. After agitation at 800 rpm, 0.6 ml VC solution was added (Supplementary Fig. 11j), and the mixture was shaken at 600–800 rpm. The resulting suspensions, designated CeO_2-(111)-VC and CeO_2-(110)-VC, were sequentially washed with high-purity ethanol, Na_2CO_3 solution and distilled water to remove residual VC and DHA, and redispersed in distilled water. Next, 0.5 ml of 50 mM $Cu(NO_3)_2$ solution was added, followed by thorough shaking. The resulting mixture was centrifuged or filtered to isolate the solid product, which was subsequently transferred to a furnace using a six-axis robotic arm (CR5A; Supplementary Fig. 32a). Calcination was conducted at 300 °C for 2 h under an inert atmosphere, yielding the final Cu_1/CeO_2-(111) and Cu_1/CeO_2-(110) samples, collectively referred to as CeO_2 C-SACs.

High-throughput synthesis of electrode-based C-SACs

We developed an integrated workflow for electrode-based C-SAC synthesis. Using Fe_1/CeO_2-VC@NF as a demonstration electrode, we first sputtered an ~30-nm CeO_2 layer onto nickel foam substrates that had been sequentially cleaned in hydrochloric acid, acetone, deionized water and ethanol. We then used a laser-cutting robot (Xtool M1) to trim the CeO_2@NF composites into 1 cm × 1.3 cm pieces. For batch processing, we fabricated a specialized metallic holder (Supplementary Fig. 32b,c), which can simultaneously secure more than 100 electrodes. A robotic arm equipped with a gripper transferred these electrodes into 0.1 M KOH for a soak, followed by cyclic voltammetry scans to activate the electrodes. After activation, the CeO_2@NF samples were immersed in 0.1 M VC solution, producing clicked CeO_2@NF (CeO_2-VC@NF). We placed these prepared electrodes on a custom 3D-printed stage (Supplementary Fig. 32d,e). The robotic arm then transported the stage to the liquid-handling robot, which dispensed and precisely controlled the volume of metal precursor solutions onto the CeO_2-VC@NF, thereby producing Fe_1/CeO_2-VC@NF. After the solvent had fully evaporated the electrodes were ready for electrochemical testing.

High-throughput electrochemical testing of electrode-based C-SACs

We implemented high-throughput electrochemical testing of electrode-based C-SACs using a robotic arm (xArm; Supplementary Fig. 34). The electrochemical measurements were conducted in a three-electrode configuration, tailored to distinct reaction conditions. For HER and OER, we utilized 160 ml of 1.0 M KOH as the electrolyte, while for UOR, we prepared a modified solution by adding 0.3333 M urea to 1.0 M KOH. The experimental setup employed a Hg/HgO (1.0 M KOH) electrode as the reference, a graphite rod as the counter electrode, and the as-synthesized C-SAC@NF as the working electrode. Linear sweep voltammograms were acquired within predetermined potential windows using a scan rate of 5 mV s^{-1}. The potential ranges for OER and UOR spanned 0.2 to 0.7 V versus Hg/HgO, while for HER, the range extended from −0.7 to −1.4 V versus Hg/HgO. We automated the sequential exchange of electrodes using the robotic arm, which accurately identified, positioned and retrieved prelabelled samples. This process was seamlessly integrated into the testing workflow, substantially reducing human intervention. For control catalysts, as-prepared Pt–C and RuO_2 powders were fabricated into electrodes with noble-metal loadings matched to those of the corresponding C-SACs.

Large-scale synthesis of C-SAC-L

The large-scale synthesis was carried out manually following the same synthetic route as the high-throughput synthesis of powder-based C-SACs, with proportional scaling-up, while accounting for concentration adjustments required by the increased container volume. All reactions were conducted in containers larger than 100 l under continuous stirring. Using this approach, Cu_1/CeO_2-(111)-L and Cu_1/CeO_2-(110)-L were synthesized, and the same procedure was applied to Ni_1/CeO_2-L, Mn_1/CeO_2-L and Ni_1/TiO_2-L by changing the metal precursors accordingly.

Synthesis of additional reference samples

Cu_x/CeO_2-1 and Cu_1/CeO_2-(111) were synthesized using similar procedures with identical CeO_2 and Cu^{2+} precursor concentrations. The key difference is that Cu_x/CeO_2-1 was prepared without the VC addition step. Cu_x/CeO_2-2 was synthesized using a fivefold higher Cu^{2+} precursor concentration to achieve a Cu content comparable to that of Cu_1/CeO_2-(111), enabling a fair comparison of catalytic performance.

To synthesize Cu-VC/CeO_2, 100 mg copper(II) nitrate trihydrate ($Cu(NO_3)_2\cdot 3H_2O$) and 100 mg VC were dissolved in 200 ml distilled water and vigorously stirred at room temperature for 6 h, resulting in a pale green Cu-VC solution. Subsequently, 400 mg CeO_2 was dispersed

into the Cu-VC solution, thoroughly washed with sodium carbonate solution and deionized water and collected by centrifugation. The solid was dried under vacuum at 80 °C for 24 h and calcined at 300 °C in an Ar atmosphere for 2 h to yield Cu-VC/CeO$_2$.

To synthesize Cu-VC and Cu-VC-C, copper(II) nitrate trihydrate (Cu(NO$_3$)$_2$·3H$_2$O, 100 mg) was dissolved in 200 ml of distilled water, after which ascorbic acid (1 g) was added. The mixture was vigorously stirred at room temperature for 6 h, producing a pale green solution. Following drying via rotary evaporation, the resulting solid was labelled Cu-VC. This solid was then calcined at 300 °C under an argon atmosphere for 2 h, yielding the final product, designated as Cu-VC-C.

For the synthesis of Cu-doped CeO$_2$, 160 ml of deionized water was added into a 200-ml beaker, followed by the addition of glucose (0.02 mol) and magnetic stirring for 30 min. Eventually, acrylamide (0.03 mol), cerium nitrate hexahydrate (0.01 mol) and copper nitrate trihydrate (0.001 mol) were sequentially added to the glucose solution, with continuous stirring for 2 h. After thorough stirring, 12 ml of ammonia solution was added dropwise to the obtained solution to adjust the pH value to a minimum of 10. During this addition, the colour of the solution intensified. The stirring continued at room temperature for 5 h to yield a homogeneous gel. The as-obtained gel was transferred to a 200-ml hydrothermal reactor and then placed in an oven at 180 °C for 72 h. Subsequently, the solid product was obtained by filtration or centrifugation and subjected to alternate washing with water and ethanol for a minimum of six times. The washed precipitate was then dried in a vacuum oven at 70 °C for 24 h. Afterwards, the product was calcined under an N$_2$ atmosphere at 600 °C for 6 h in a tube furnace, with a heating rate of 5 °C min^{-1}, and the product was calcined further in a muffle furnace at 400 °C for 4 h to obtain flower-shaped Cu-doped CeO$_2$.

For the synthesis of Cu/CeO$_2$-H$_2$, CeO$_2$ powder was treated in a tubular furnace under high-purity H$_2$ flow (100 ml min^{-1}) at 300 °C for 2 h, then cooled to room temperature under H$_2$ to obtain CeO$_2$-H$_2$. CeO$_2$-H$_2$ (400 mg) was redispersed in deionized water (100 ml) with stirring and Cu(NO$_3$)$_2$·3H$_2$O (100 mg) was added. After 6 h of stirring, the solid was collected by centrifugation or filtration and calcined at 300 °C for 2 h under an inert atmosphere to yield Cu/CeO$_2$-H$_2$.

Catalyst characterization

The crystal phase, morphology and microstructure of the samples were analysed using X-ray diffraction with a Rigaku Dmax-2400 instrument operated at 40 kV and 40 mA using Cu-Kα radiation. ^{1}H NMR spectra were collected at 298 K on a Bruker AVANCE III HD 400 MHz spectrometer, with tetramethylsilane serving as the internal reference. The surface characteristics of the SACs were studied using HAADF-STEM, allowing for sub-ångstrom-scale resolution. The HAADF-STEM images were acquired using an FEI Titan Cubed Themis G2 300 spherical AC STEM at the Electron Microscopy Laboratory of Peking University. The carbon content was quantified with a LECO CS-230 carbon/sulfur analyser. Samples were completely combusted in an O$_2$ stream, converting carbon to CO and CO$_2$; the resulting gases were measured by infrared absorption spectroscopy. In situ Raman measurements were performed in a custom-built cell on a WITec Alpha300 R microscope equipped with a 532-nm laser. Electron paramagnetic resonance spectra were obtained on a Bruker EMXplus-6/1 spectrometer operating at 9.4 GHz and 6.34 mW to quantify oxygen vacancies. UV–visible diffuse reflectance spectra were measured on a Shimadzu UV-3600i Plus spectrophotometer equipped with an integrating sphere. Cu contents were determined by inductively coupled plasma optical emission spectroscopy (Agilent 7700). NH$_3$-TPD and O$_2$-TPD experiments were performed on automatic chemical adsorption analysers, namely the ChemBET Pulsar TPR/TPD (Quantachrome Instruments) and the AUTOCHEM II 2920. XAFS spectra were collected at the 1W1B beamline of the Beijing Synchrotron Radiation Facility, beamline BL14W1 of the Shanghai Synchrotron Radiation Facility and the XAFCA beamline of the Singapore Synchrotron Light Source. The acquired data were analysed using the Athena and Artemis modules from the IFEFFIT software package.

Computational methods

DFT-VASP methods. Spin-polarized DFT calculations in this work were carried out using the Vienna ab initio simulation package (VASP)[70–72]. The Perdew–Burke–Ernzerhof (PBE) functional under the generalized gradient approximation was employed to evaluate the electron exchange-correlation energy[73]. Meanwhile, the projector augmented wave method was used to capture interactions between atomic nuclei and outer electrons[74], with a plane-wave kinetic energy cutoff of 500 eV. To account for long-range dispersion interactions, Grimme's DFT-D2 method[75] was adopted, thereby ensuring reliable treatment of adsorbate–surface interactions[76]. To more accurately describe the 4f electron shell of Ce, a Hubbard U value of 4.5 eV ($U_{eff} = U - J$, $J = 0$) was applied to correct the Ce 4f orbitals[77–79]. Additionally, a Hubbard U value of 6 eV was employed to correct the Cu 3d electrons[80,81]. Brillouin-zone sampling was performed using the Gaussian smearing method with a smearing width of 0.05 eV. Geometric optimizations utilized a conjugate gradient algorithm, converged when residual forces on each atom were less than 0.03 eV/Å (for each direction), and the total energy was converged to 10^{-5} eV. Only the Γ point was used for sampling the first Brillouin zone. The LOBSTER program was employed to compute the crystal orbital Hamilton population for bonding-state analysis[82].

For a given reaction (A→B), the reaction free energy ΔG (including contributions from the DFT total energy, zero-point energy, vibrational enthalpy (thermal corrections) and vibrational entropy) is defined as:

$$\Delta G = G_B - G_A \qquad (1)$$

where G_A and G_B denote the Gibbs free energies of the initial state (A) and final state (B), respectively. Supercells were prepared by cleaving optimized CeO$_2$ along the (111) and (110) planes. For both the (111) and (110) surfaces, periodic slab models were constructed containing 48 Ce and 96 O atoms, and an 18-Å vacuum layer was introduced along the z direction to eliminate spurious periodic interactions. A pseudo-hydrogen passivation strategy[83] was adopted to saturate the dangling bonds arising from exposed Ce/O atoms at the bottom of the slabs. During optimization of the pseudo-hydrogen positions, Ce and O atoms in the bottom region were fixed at their bulk coordinates.

The CI-NEB method[84] was again used to locate transition states for elementary surface reactions, verified by a single imaginary frequency. The activation energy E_a was calculated as the energy difference between the transition state and the intermediate state. For geometry optimization of these transition states, the atomic structure was relaxed until the forces on each atom were below 0.05 eV/Å.

Dmol^3 methods. To gain deeper insight into the interaction mechanisms between clicking auxiliaries and the catalyst support surface, we performed additional calculations using a cluster model and numerical basis sets. Specifically, we employed the same PBE functional[73] and a double-numerical basis set as implemented in the DMol^3 package[85,86]. We applied a global orbital cutoff radius of 5.6 Å, with adsorption geometries fully optimized until total energy convergence of 10^{-5} Ha and atomic force convergence of 0.005 Ha/Å were achieved. Gaussian smearing was employed with a width of $\sigma = 0.005$ Ha. As calculations were based on a cluster model, k-space sampling and vacuum layers were not required. Dispersion corrections were accounted for using the Tkatchenko–Scheffler DFT-D method[87].

For modelling the interaction of VC with CeO$_2$, we constructed a Ce$_6$O$_{12}$ cluster model, where edge sites were terminated by hydroxyl groups. VC adsorption was modelled by placing a single VC molecule onto the CeO$_2$ cluster and performing full geometry optimization.

Cu^{2+} adsorption and anchoring were studied by positioning an isolated Cu^{2+} ion (initial spin = 1.0) initially far from the CeO$_2$ cluster to

establish a reference state. This reference strategy minimizes potential inaccuracies arising from the finite basis set size and was similarly applied in VC adsorption calculations. Comparative analyses were performed for Cu^{2+} adsorption on electron-enriched CeO_2 and pristine CeO_2 clusters. Relative energies for each configuration were calculated against the corresponding reference states to determine reaction energies for each adsorption step.

To quantify the strength of interaction between a molecule and the metal oxide surface, we define the adsorption energy (E_{ads}) as follows:

$$E_{ads} = E_M + E_{surface} - E_{M/surface} \qquad (2)$$

where E_{ads} denotes the adsorption energy, $E_{M/surface}$ is the total energy of the adsorbed molecule–surface system, and E_M and $E_{surface}$ are the total energies of the isolated molecule and the clean metal oxide surface, respectively.

AIMD methods. We performed AIMD simulations using VASP to explore the adsorption dynamics of the clicking-auxiliary VC molecule on the CeO_2 or TiO_2 surface and its role in anchoring metal ions. To achieve a balance between computational efficiency and accuracy, we adapted the computational framework described in the DFT methods, modifying parameters specifically for AIMD. We expanded the wavefunctions using a plane-wave basis set with a 400-eV cutoff energy and applied Gaussian smearing with a width of 0.2 eV to enhance numerical stability, and spin polarization was implemented.

We constructed the CeO_2 surface model by cleaving two atomic layers from the (111) facet and introducing a 14-Å vacuum layer to avoid periodic interactions. To simulate the solution-phase environment, we placed 35 water molecules combined with a VC molecule, two $Na_2(CO_3)_2$, a $Cu(NO_3)_2$ molecule, a $Fe(NO_3)_3$ or a $Pt(NO_3)_2$ molecule within the vacuum region, respectively. In the TiO_2 system, we constructed the TiO_2 surface model by cleaving two atomic layers from the (101) facet and introducing a 16-Å vacuum layer. To simulate the solution-phase environment, we placed 40 water molecules combined with a VC molecule, two $Na_2(CO_3)_2$, a $Cu(NO_3)_2$ molecule or a $Fe(NO_3)_3$ within the vacuum region, respectively. We optimized the structure by setting energy and force convergence criteria to 10^{-4} eV and 0.05 eV/Å, respectively, ensuring a highly accurate initial configuration. Due to the model's size, we sampled only the Γ-point in the Brillouin zone to maintain computational efficiency.

After optimizing the structure, we gradually heated the system from 0 K to 298 K over 1.49 ps using velocity scaling and equilibrated it at 298 K for an additional 2 ps with a 1-fs time step to ensure thermal stability. We simulated the dynamic adsorption and Cu anchoring processes by performing constrained AIMD simulations with the slow-growth method. We defined the collective variable as a combination of distances between the Cu atom and the O atoms in both VC and CeO_2 and incrementally increased it by 0.005 Å per molecular dynamics step. We recorded the energy at each step and smoothed the trajectory using the Savitzky–Golay method to highlight key trends in the energy profile.

Data availability

Relevant data supporting the key findings of this study are available within the article and Supplementary Information. Source data are provided with this paper.

References

1. Hung, S.-F. et al. A metal-supported single-atom catalytic site enables carbon dioxide hydrogenation. *Nat. Commun.* **13**, 819 (2022).
2. Liu, J. et al. Electrochemical conversion of small organic molecules to value-added chemicals and hydrogen/electricity without CO_2 emission: electrocatalysts, devices and mechanisms. *eScience* **5**, 100267 (2025).
3. Li, J., Stephanopoulos, M. F. & Xia, Y. Introduction: heterogeneous single-atom catalysis. *Chem. Rev.* **120**, 11699–11702 (2020).
4. Chandrashekhar, V. G., Baumann, W., Beller, M. & Jagadeesh, R. V. Nickel-catalyzed hydrogenative coupling of nitriles and amines for general amine synthesis. *Science* **376**, 1433–1441 (2022).
5. Jagadeesh, R. V. et al. MOF-derived cobalt nanoparticles catalyze a general synthesis of amines. *Science* **358**, 326–332 (2017).
6. Lazaridou, A. et al. Recognizing the best catalyst for a reaction. *Nat. Rev. Chem.* **7**, 287–295 (2023).
7. Han, C. et al. Metal–support interaction in single-atom electrocatalysts: a perspective of metal oxide supports. *eScience* **4**, 100269 (2024).
8. Jagadeesh, R. V. et al. Nanoscale Fe_2O_3-based catalysts for selective hydrogenation of nitroarenes to anilines. *Science* **342**, 1073–1076 (2013).
9. Fan, M. et al. Single-site decorated copper enables energy- and carbon-efficient CO_2 methanation in acidic conditions. *Nat. Commun.* **14**, 3314 (2023).
10. Wang, X. et al. Efficient electrosynthesis of *n*-propanol from carbon monoxide using a Ag–Ru–Cu catalyst. *Nat. Energy* **7**, 170–176 (2022).
11. Shi, Z. et al. Phase-dependent growth of Pt on MoS_2 for highly efficient H_2 evolution. *Nature* **621**, 300–305 (2023).
12. Liu, L. & Corma, A. Metal catalysts for heterogeneous catalysis: from single atoms to nanoclusters and nanoparticles. *Chem. Rev.* **118**, 4981–5079 (2018).
13. Qin, J. et al. Altering ligand fields in single-atom sites through second-shell anion modulation boosts the oxygen reduction reaction. *J. Am. Chem. Soc.* **144**, 2197–2207 (2022).
14. Han, L. et al. Local modulation of single-atomic Mn sites for enhanced ambient ammonia electrosynthesis. *ACS Catal.* **11**, 509–516 (2021).
15. Han, L. et al. Design of Ru-Ni diatomic sites for efficient alkaline hydrogen oxidation. *Sci. Adv.* **8**, eabm3779 (2022).
16. Hai, X. et al. Scalable two-step annealing method for preparing ultra-high-density single-atom catalyst libraries. *Nat. Nanotechnol.* **17**, 174–181 (2022).
17. Hai, X. et al. Geminal-atom catalysis for cross-coupling. *Nature* **622**, 754–760 (2023).
18. Gu, J. et al. Single-atom catalysts with anionic metal centers: promising electrocatalysts for the oxygen reduction reaction and beyond. *J. Energy Chem.* **63**, 285–293 (2021).
19. Lin, S., Xu, H., Wang, Y., Zeng, X. C. & Chen, Z. Directly predicting limiting potentials from easily obtainable physical properties of graphene-supported single-atom electrocatalysts by machine learning. *J. Mater. Chem. A* **8**, 5663–5670 (2020).
20. Yu, L. et al. Double-atom catalysts featuring inverse sandwich structure for CO_2 reduction reaction: a synergetic first-principles and machine learning investigation. *ACS Catal.* **13**, 9616–9628 (2023).
21. Liu, C. et al. Single-boron catalysts for nitrogen reduction reaction. *J. Am. Chem. Soc.* **141**, 2884–2888 (2019).
22. DeRita, L. et al. Structural evolution of atomically dispersed Pt catalysts dictates reactivity. *Nat. Mater.* **18**, 746–751 (2019).
23. Wang, H. et al. Surpassing the single-atom catalytic activity limit through paired Pt-O-Pt ensemble built from isolated Pt_1 atoms. *Nat. Commun.* **10**, 3808 (2019).
24. Yan, M. et al. Rational design of graphene-supported single-atom catalysts for electroreduction of nitrogen. *Inorg. Chem.* **60**, 18314–18324 (2021).
25. Yan, M. et al. Single-iron supported on defective graphene as efficient catalysts for oxygen reduction reaction. *J. Phys. Chem. C* **124**, 13283–13290 (2020).

26. Wu, Z.-Y. et al. A general synthesis of single atom catalysts with controllable atomic and mesoporous structures. *Nat. Synth.* **1**, 658–667 (2022).

27. Xia, C. et al. General synthesis of single-atom catalysts with high metal loading using graphene quantum dots. *Nat. Chem.* **13**, 887–894 (2021).

28. Zheng, T. et al. Large-scale and highly selective CO_2 electrocatalytic reduction on nickel single-atom catalyst. *Joule* **3**, 265–278 (2019).

29. Wang, L. et al. Atomic-level insights in optimizing reaction paths for hydroformylation reaction over Rh/CoO single-atom catalyst. *Nat. Commun.* **7**, 14036 (2016).

30. Wang, L. et al. Supported rhodium catalysts for ammonia–borane hydrolysis: dependence of the catalytic activity on the highest occupied state of the single rhodium atoms. *Angew. Chem. Int. Ed. Engl.* **56**, 4712–4718 (2017).

31. Ge, X. et al. Palladium single atoms on TiO_2 as a photocatalytic sensing platform for analyzing the organophosphorus pesticide chlorpyrifos. *Angew. Chem. Int. Ed. Engl.* **59**, 232–236 (2020).

32. Han, L. et al. Modulating single-atom palladium sites with copper for enhanced ambient ammonia electrosynthesis. *Angew. Chem. Int. Ed. Engl.* **60**, 345–350 (2021).

33. Lang, R. et al. Non defect-stabilized thermally stable single-atom catalyst. *Nat. Commun.* **10**, 234 (2019).

34. Zhang, Z. et al. Thermally stable single atom Pt/m-Al_2O_3 for selective hydrogenation and CO oxidation. *Nat. Commun.* **8**, 16100 (2017).

35. Li, X. et al. Construction of Ru single-atoms on ceria to reform the products of CO_2 photoreduction. *ACS Nano* **18**, 5741–5751 (2024).

36. He, X. et al. Engineering a self-grown TiO_2/Ti-MOF heterojunction with selectively anchored high-density Pt single-atomic cocatalysts for efficient visible-light-driven hydrogen evolution. *Angew. Chem. Int. Ed. Engl.* **62**, e202217439 (2023).

37. Lang, R. et al. Single-atom catalysts based on the metal–oxide interaction. *Chem. Rev.* **120**, 11986–12043 (2020).

38. Yang, X.-F. et al. Single-atom catalysts: a new frontier in heterogeneous catalysis. *Acc. Chem. Res.* **46**, 1740–1748 (2013).

39. Han, L. et al. A single-atom library for guided monometallic and concentration-complex multimetallic designs. *Nat. Mater.* **21**, 681–688 (2022).

40. Han, G.-F. et al. Abrading bulk metal into single atoms. *Nat. Nanotechnol.* **17**, 403–407 (2022).

41. Ji, S. et al. Chemical synthesis of single atomic site catalysts. *Chem. Rev.* **120**, 11900–11955 (2020).

42. Wei, Y.-S., Zhang, M., Zou, R. & Xu, Q. Metal–organic framework-based catalysts with single metal sites. *Chem. Rev.* **120**, 12089–12174 (2020).

43. Kolb, H. C., Finn, M. G. & Sharpless, K. B. Click chemistry: diverse chemical function from a few good reactions. *Angew. Chem. Int. Ed. Engl.* **40**, 2004–2021 (2001).

44. Zhao, J. et al. Radical-mediated click-clip reactions. *Science* **385**, 1354–1359 (2024).

45. Morris, R. E. Clicking zeolites together. *Science* **379**, 236–237 (2023).

46. DeForest, C. A., Polizzotti, B. D. & Anseth, K. S. Sequential click reactions for synthesizing and patterning three-dimensional cell microenvironments. *Nat. Mater.* **8**, 659–664 (2009).

47. Chen, Z.-J. et al. Exploiting antisite defects in $FeWN_2$ nanosheets for enol electro-oxidation coupled with H_2 evolution at a large current density. *Angew. Chem. Int. Ed. Engl.* **64**, e202500678 (2025).

48. Chen, Z.-J. et al. Acidic enol electrooxidation-coupled hydrogen production with ampere-level current density. *Nat. Commun.* **14**, 4210 (2023).

49. Schmitt, R. et al. A review of defect structure and chemistry in ceria and its solid solutions. *Chem. Soc. Rev.* **49**, 554–592 (2020).

50. Weber, W. H., Hass, K. C. & McBride, J. R. Raman study of CeO_2: second-order scattering, lattice dynamics, and particle-size effects. *Phys. Rev. B* **48**, 178–185 (1993).

51. Ziemba, M., Schilling, C., Ganduglia-Pirovano, M. V. & Hess, C. Toward an atomic-level understanding of ceria-based catalysts: when experiment and theory go hand in hand. *Acc. Chem. Res.* **54**, 2884–2893 (2021).

52. Trindade, F. J. et al. Tuning of shape, defects, and disorder in lanthanum-doped ceria nanoparticles: implications for high-temperature catalysis. *ACS Appl. Nano Mater.* **5**, 8859–8867 (2022).

53. Sun, H., Wang, H. & Qu, Z. Construction of CuO/CeO_2 catalysts via the ceria shape effect for selective catalytic oxidation of ammonia. *ACS Catal.* **13**, 1077–1088 (2023).

54. Khivantsev, K. et al. Transforming ceria into 2D clusters enhances catalytic activity. *Nature* **640**, 947–953 (2025).

55. Li, Y. et al. Boron doping-induced ultrahigh Ce^{3+} ratio in amorphous CeO_2/GO catalyst for low-concentration CO_2 photoreduction. *Angew. Chem. Int. Ed. Engl.* **64**, e202505668 (2025).

56. Zu, D. et al. Oxygen vacancies trigger rapid charge transport channels at the engineered interface of S-scheme heterojunction for boosting photocatalytic performance. *Angew. Chem. Int. Ed. Engl.* **63**, e202405756 (2024).

57. Zhang, P. et al. Surface Ru–H bipyridine complexes-grafted TiO_2 nanohybrids for efficient photocatalytic CO_2 methanation. *J. Am. Chem. Soc.* **145**, 5769–5777 (2023).

58. Zhou, W. et al. Visible-light-driven oxidation of benzene to phenol with O_2 over photoinduced oxygen-vacancy-rich WO_3. *Angew. Chem. Int. Ed. Engl.* **137**, e202417703 (2025).

59. Ma, S. et al. Photocatalytic hydrogen production on a sp^2-carbon-linked covalent organic framework. *Angew. Chem. Int. Ed. Engl.* **61**, e202208919 (2022).

60. Szymanski, N. J. et al. An autonomous laboratory for the accelerated synthesis of novel materials. *Nature* **624**, 86–91 (2023).

61. Grabowski, P., Fabjanowicz, B., Podgórska, M., Rogóż, M. & Wasylczyk, P. Automated photo-aligned liquid crystal elastomer film fabrication with a low-tech, home-built robotic workstation. *Sci. Rep.* **12**, 17598 (2022).

62. Li, M. et al. Single-atom tailoring of platinum nanocatalysts for high-performance multifunctional electrocatalysis. *Nat. Catal.* **2**, 495–503 (2019).

63. Fei, H. et al. General synthesis and definitive structural identification of MN_4C_4 single-atom catalysts with tunable electrocatalytic activities. *Nat. Catal.* **1**, 63–72 (2018).

64. Li, Y. et al. Selective light absorber-assisted single nickel atom catalysts for ambient sunlight-driven CO_2 methanation. *Nat. Commun.* **10**, 2359 (2019).

65. Li, Y. et al. Facile top-down strategy for direct metal atomization and coordination achieving a high turnover number in CO_2 photoreduction. *J. Am. Chem. Soc.* **142**, 19259–19267 (2020).

66. Wang, T. et al. CO oxidation over $Pt/Cr^{3+}Fe_{0.7}O_3$ catalysts: enhanced activity on single Pt atom by H_2O promotion. *J. Catal.* **382**, 192–203 (2020).

67. Xie, S. et al. Pt atomic single-layer catalyst embedded in defect-enriched ceria for efficient CO oxidation. *J. Am. Chem. Soc.* **144**, 21255–21266 (2022).

68. Chen, W. & Xu, S. Unraveling the complete mechanism of the NH_3-selective catalytic reduction of NO over CeO_2. *ACS Catal.* **13**, 15481–15492 (2023).

69. Chen, W. et al. How do the morphology and crystal facet of CeO$_2$ determine the catalytic activity toward NO removal? *Small* **21**, 2407805 (2025).

70. Kresse, G. & Furthmüller, J. Efficient iterative schemes for ab initio total-energy calculations using a plane-wave basis set. *Phys. Rev. B* **54**, 11169–11186 (1996).

71. Kresse, G. & Furthmüller, J. Efficiency of ab-initio total energy calculations for metals and semiconductors using a plane-wave basis set. *Comput. Mater. Sci.* **6**, 15–50 (1996).

72. Kresse, G. & Hafner, J. Ab initio molecular dynamics for open-shell transition metals. *Phys. Rev. B* **48**, 13115–13118 (1993).

73. Perdew, J. P., Burke, K. & Ernzerhof, M. Generalized gradient approximation made simple. *Phys. Rev. Lett.* **77**, 3865–3868 (1996).

74. Blöchl, P. E. Projector augmented-wave method. *Phys. Rev. B* **50**, 17953–17979 (1994).

75. Grimme, S. Semiempirical GGA-type density functional constructed with a long-range dispersion correction. *J. Comput. Chem.* **27**, 1787–1799 (2006).

76. Xu, S. & Carter, E. A. Oxidation state of GaP photoelectrode surfaces under electrochemical conditions for photocatalytic CO$_2$ reduction. *J. Phys. Chem. B* **124**, 2255–2261 (2020).

77. Kildgaard, J. V., Hansen, H. A. & Vegge, T. DFT+U study of strain-engineered CO$_2$ reduction on a CeO$_{2-x}$ (111) facet. *J. Phys. Chem. C* **125**, 14221–14227 (2021).

78. Wu, T., Deng, Q., Hansen, H. A. & Vegge, T. Mechanism of water splitting on gadolinium-doped CeO$_2$(111): a DFT+U study. *J. Phys. Chem. C* **123**, 5507–5517 (2019).

79. Su, Y.-Q., Liu, J.-X., Filot, I. A. W., Zhang, L. & Hensen, E. J. M. Highly active and stable CH$_4$ oxidation by substitution of Ce^{4+} by two Pd^{2+} ions in CeO$_2$(111). *ACS Catal.* **8**, 6552–6559 (2018).

80. Xiong, W. et al. Fine cubic Cu$_2$O nanocrystals as highly selective catalyst for propylene epoxidation with molecular oxygen. *Nat. Commun.* **12**, 5921 (2021).

81. Isseroff, L. Y. & Carter, E. A. Importance of reference Hamiltonians containing exact exchange for accurate one-shot *GW* calculations of Cu$_2$O. *Phys. Rev. B* **85**, 235142 (2012).

82. Maintz, S., Deringer, V. L., Tchougréeff, A. L. & Dronskowski, R. LOBSTER: a tool to extract chemical bonding from plane-wave based DFT. *J. Comput. Chem.* **37**, 1030–1035 (2016).

83. Xu, S. & Carter, E. A. CO$_2$ photoelectrochemical reduction catalyzed by a GaP(001) photoelectrode. *ACS Catal.* **11**, 1233–1241 (2021).

84. Henkelman, G., Uberuaga, B. P. & Jónsson, H. A climbing image nudged elastic band method for finding saddle points and minimum energy paths. *J. Chem. Phys.* **113**, 9901–9904 (2000).

85. Delley, B. An all-electron numerical method for solving the local density functional for polyatomic molecules. *J. Chem. Phys.* **92**, 508–517 (1990).

86. Delley, B. From molecules to solids with the DMol^3 approach. *J. Chem. Phys.* **113**, 7756–7764 (2000).

87. Tkatchenko, A. & Scheffler, M. Accurate molecular van der Waals interactions from ground-state electron density and free-atom reference data. *Phys. Rev. Lett.* **102**, 073005 (2009).

Acknowledgements

Author contributions

The work was conceived by W.C., R. Zou, J. Li, J. Lu and J.Z. with input from all authors. Methodology was developed by W.C. and L.F., with software contributions from B.M. and L.Z. Validation was performed by S.W. and Z.D. Formal analysis was carried out by W.C., S.X. and S.W., while W.C. and X.H. conducted the investigation. Resources were provided by Z.D., F.M. and R. Zhong. Data curation was handled by B.M. and L.F. The original draft was prepared by W.C. and S.W., and the paper was reviewed and edited by R. Zou and J. Li. Visualization was conducted by W.C., L.Z. and B.M. Supervision was provided by R. Zou, J. Li and J. Lu.

Competing interests

The authors declare no competing interests.

Additional information

Supplementary information The online version contains supplementary material available at https://doi.org/10.1038/s44160-026-01004-9.

Correspondence and requests for materials should be addressed to Shengyao Wang, Jiong Lu, Ju Li or Ruqiang Zou.

Peer review information *Nature Synthesis* thanks Sang Hoon Joo, Botao Qiao and the other, anonymous, reviewer(s) for their contribution to the peer review of this work. Primary Handling Editor: Peter Seavill, in collaboration with the *Nature Synthesis* team.

Reprints and permissions information is available at www.nature.com/reprints.